*metals*

MDPI

*Article*

# Influence of Th, Zr, and Ti Dopants on Solution Property of Xe in Uranium Dioxide with Defects: A DFT + U Study

**Liu Pan [1], Zhen Wang [2,*], Qingqing Wang [2], Zhixiao Liu [3,*], Min Pan [4], Zheng Huang [1,*] and Lu Wu [3]**

[1] School of Physical Science Technology, Southwest Jiaotong University, Chengdu 610031, China; 2019201031@my.swjtu.edu.cn
[2] The First Sub-Institute, Nuclear Power Institute of China, Chengdu 610041, China; wqq1132675279@163.com
[3] College of Materials Science and Engineering, Hunan University, Changsha 410082, China; wulu1002@126.com
[4] Superconductivity and New Energy R&D Center, Southwest Jiaotong University, Chengdu 610031, China; mpan@swjtu.edu.cn
* Correspondence: wangzshu@126.com (Z.W.); zxliu@hnu.edu.cn (Z.L.); zhhuang@swjtu.edu.cn (Z.H.)

**Abstract:** To ensure the safety and efficient operation of nuclear reactors, it is imperative to understand the effects of various dopants (Ti, Th, and Zr) on the solubility of the fission product Xe in $UO_2$. In this study, Hubbard corrected density functional theory (DFT + U) and occupation matrix control were used to investigate the bulk and defect properties of $UO_2$. The results show that the $UO_2$-Ti system is more favorable for Xe dissolution in vacancies, whereas the $UO_2$-Th system has little effect on the dissolution of Xe atoms. Th, Zr, and Ti inhibit the aggregation of Xe clusters, and Ti is the least favorable for the nucleation and growth of Xe clusters.

**Keywords:** $UO_2$; fission gas; dopant; vacancy; DFT simulation



**Citation:** Pan, L.; Wang, Z.; Wang, Q.; Liu, Z.; Pan, M.; Huang, Z.; Wu, L. Influence of Th, Zr, and Ti Dopants on Solution Property of Xe in Uranium Dioxide with Defects: A DFT + U Study. *Metals* **2022**, *12*, 879. https://doi.org/10.3390/met12050879

Academic Editor: Enrique Jimenez-Melero

Received: 23 March 2022
Accepted: 10 May 2022
Published: 23 May 2022



## 1. Introduction

Nuclear energy has been regarded as the most promising energy for the future, and its development has attracted significant attention. Uranium dioxide ($UO_2$) is the preferred fuel for light–water reactors (LWRs), and its properties play an important role in the reliability and safety of nuclear reactors. Over the past century, numerous experimental and theoretical studies have been conducted on the structure and properties of uranium dioxide ($UO_2$) under irradiation. Xenon (Xe) is the product of uranium fission during reactor operations [1,2]. Xe released into the helium-filled gap of wrapping materials can reduce the thermal conductivity of the fueled gap and increase the pressure of the ventilation system. In addition, Xe release can generate stress on the cladding, resulting in the mechanical degradation of structural materials in fuel components [3,4]. Fission gas also tends to accumulate and form bubbles in the interior of nuclear fuel, resulting in expansion, microstructural change, and performance degradation, which affect the safety of nuclear reactors [5–8]. To improve the physical, chemical, and thermodynamic properties of nuclear fuel in the ground state and reduce the release of fission gas during fuel irradiation, many dopants, such as niobium (Nb) [9,10], magnesium (Mg) [11,12], titanium (Ti) [13,14], chromium (Cr) [15,16] and zirconium (Zr) [17,18] have been studied in the past decades. Several studies have reported that Zr doping can improve the performance of $UO_2$ nuclear fuels. Zr doping can reduce the swelling rate of $UO_2$ fuel and improve its high-temperature water corrosion resistance [19]. Ti doping can enhance the sinterability and grain size of $UO_2$ [20]. Thorium (Th) doping can improve the antioxidant capacity of $UO_2$ and guarantee long-term storage [21]. However, few studies have been conducted on the effects of Ti, Th, and Zr on Xe solubility in $UO_2$ fuel. Therefore, further research on the doping effect of these metals is required to effectively analyze nuclear fuel performance.

There is a lack of sufficient experimental data owing to the high cost of radioactive $UO_2$ fuel and related irradiation, and existing data are decades old. However, with the

advancement of computers, using computational methods as an effective complement to experiments can enhance the understanding of fission gas behavior in $UO_2$-based nuclear materials. For instance, density-functional-theory (DFT)-based first-principles calculations [22,23] have been widely used in many atomic-scale simulations of $UO_2$ nuclear materials. In particular, the stable site occupation and diffusion behavior of fission gas Xe in $UO_2$ have been extensively studied. During the initial stages of the fuel life cycle, noble gas atoms can occupy the empty octahedral sites in the $UO_2$ lattice [24]. However, as the fission reaction of $UO_2$ progresses and bombardment continues, Frenkel defects consisting of uranium and oxygen vacancies are formed in $UO_2$. Subsequently, these Frenkel defects form Schottky defects in the $UO_2$ lattice through diffusion and other methods [25,26]. The release of fission gas in $UO_2$ is characterized by point defects, dislocations, voids, and bubbles, which further leads to nuclear fuel swelling. Yu et al. [27] studied the stable occupation of Xe in $UO_2$ using the DFT + U method and found that Xe was more likely to occupy the Schottky defect position. Nerikar et al. [28] analyzed the stability of charged defects by considering various defect charge states. However, they found that the formation energies of the neutral complexes highly correlate with the experimental values than those of the charged complexes.

In this study, the $UO_2$ model was validated using the DFT + U method, and the $U_{eff}$ value is thus determined. Additionally, the occupation matrix control (OMCs) scheme was adopted to ensure that the subsequent calculations regarding the defect system can converge to the ground state. The effects of Th, Zr, and Ti on the dissolution and nucleation of Xe atoms in $UO_2$ were also studied. The electron charge density diagram of the doped system was comprehensively analyzed, and the Xe aggregation behavior in uranium vacancies was studied.

## 2. Computational Details

The DFT calculations in this study were performed on VASP (the Vienna ab-initio simulation package) [29]. The electron wave function was calculated using the projector-augmented-wave (PAW) method [30,31]. The generalized gradient approximation (GGA) [32] describes the exchange-correlation potential between electrons in the Perdew–Burke-Ernzerhof form. The cutoff energy of the plane wave was 500 eV according to the convergence tests. The Brillouin zone was sampled using the Monkhorst–Pack [33] method with a $4 \times 4 \times 4$ *k*-point mesh. The distribution function of the integral in the inverted space was a Gaussian function, and the Gaussian smearing was set to 0.05 eV. Convergence was achieved when the total energies converged within $1 \times 10^{-5}$ eV and the Hellmann–Feynman forces on each ion were lower than 0.01 eVÅ$^{-1}$. Complete geometric optimization of the $UO_2$ supercells was allowed during relaxation, without any volume or symmetry restrictions. The relaxation of the magnetic moment was limited to collinear. Spin-orbit coupling was not considered because the expected effect on the results was negligible [34].

$UO_2$ is a conventional Mott insulator [35]; however, if the DFT-based plane-wave pseudopotential method with local density approximation (LDA) or GGA [36,37] is used, it will be predicted as a metal. Owing to the strong correlation effect between the 5f electrons of the U atom in $UO_2$, traditional LDA or GGA cannot adequately describe the electronic structure. Therefore, the DFT + U method is commonly used for correction calculation [38]. Dudarev et al. [39] and Yu et al. [27] studied the basic structural properties of $UO_2$ using DFT + U, and the calculated results correlated well with the experimental data, indicating the accuracy of the method. Although point defects and defect clusters in bulk $UO_2$ and the stable occupation of Xe in $UO_2$ have been extensively studied using DFT + U, the results vary widely. This is mainly attributed to the existence of metastable states [40]. OMC and U-ramping are employed to achieve accurate DFT + U calculations and ensure that the results converge to the ground state of the system. Solomon et al. [41] found that the values calculated using the OMC method were lower than those obtained using the U-ramping method. Therefore, in this study, the occupation matrix of the U atom is initialized with the occupation matrix obtained in the $UO_2$ ground state in all subsequent calculations, and the

entire effect related to the inert gas is captured in the subsequent unconstrained structural optimization.

In $UO_2$, Jahn–Teller distortion is directly related to the direction of the magnetic moment of the uranium atom. The experimental results show that $UO_2$ is a nonlinear 3 *k* AFM system, and the magnetic moment direction of the U atom is <111> [42]. The 3 *k* AFM configuration is challenging to implement in the calculation; however, the existing results show that the 1 *k* AFM system can provide accurate results, and the calculation results are similar to those of the 3 *k* AFM system [42]. Therefore, the 1 *k* AFM system was used to describe the magnetic order of $UO_2$ in this study. The defects were constructed based on a $2 \times 2 \times 2$ $UO_2$ supercell, including 32 U atoms and 64 O atoms. There are many inherent defects in $UO_2$, including interstitial atoms, oxygen vacancies, uranium vacancies, divacancies (consisting of a uranium vacancy and the nearest oxygen vacancy), and Schottky defects (composed of one uranium vacancy and two nearest oxygen vacancies). There were three different configurations, as shown in Figure 1. In the figure, the point vacancies and vacancy clusters are represented by Int, Vo, Vu, Di, SD1, SD2, and SD3.

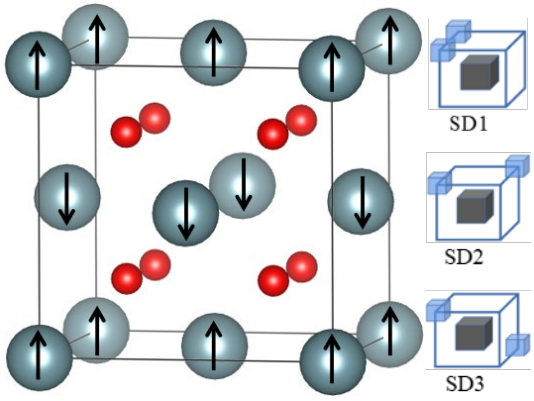


**Figure 1.** Structure of $UO_2$ and Schottky defect configuration. The red and grey balls are oxygen and uranium atoms, respectively. The arrows on the uranium atoms illustrate the magnetic moment directions in a 1 *k* spin-polarized AFM state. Black means uranium vacancies and blue means oxygen vacancies.

To investigate the interaction between dopants and Xe, the influence of dopants on the solution energy of Xe was evaluated. The solution energy is defined as the sum of the formation and incorporation energies, as first proposed by Grimes and Catlow [43]. The incorporation energy ($E_I$) is defined as

$$E_I = E_{tot}(\mathrm{Xe}) - E_{vacancy} - E_{\mathrm{Xe}} \quad (1)$$

where $E_{tot}(\mathrm{Xe})$ is the total energy of the system after Xe is adsorbed on a vacancy defect, $E_{vacancy}$ is the total energy when there is a vacancy defect in the cell, and $E_{\mathrm{Xe}}$ is the chemical potential of an isolated Xe atom. The solution energy ($E_S$) of Xe in the cell is calculated as

$$E_S = E_{tot}(\mathrm{Xe}) + n_{\mathrm{U}}\mu_{\mathrm{U}} + n_{\mathrm{O}}\mu_{\mathrm{O}} - E_{pri.} - E_{\mathrm{Xe}} \quad (2)$$

where $E_S$ is the solution energy required for Xe to dissolve into a vacancy defect. $n_{\mathrm{U}}$ and $n_{\mathrm{O}}$ are the numbers of U and O atoms missing from the defect-containing unit cell relative to the defect-free original unit cell, respectively, $\mu_{\mathrm{U}}$ and $\mu_{\mathrm{O}}$ are the chemical potentials of U and O atoms, respectively, and $E_{pri.}$ is the energy of the original cell.

As the nuclear fuel reaction progresses, uranium atoms are continuously consumed, and the oxide with the lowest uranium chemical potential undergoes a phase transition from $UO_2$ to $UO_3$. This may imply that the gradual transition of $UO_2$ to a highly oxidized phase prompts a corresponding increase in the chemical potential of oxygen in uranium oxide. Therefore, the chemical potential of each atom must be carefully selected based on

environmental conditions and possible phases to determine the energy associated with the $UO_2$ defect. The energy of the atomic chemical potential can be calculated using DFT as:

$$\mu(T = 0) \approx E^{total} \tag{3}$$

The chemical potential of uranium and oxygen, and the chemical potential of $UO_2$, can be expressed as:

$$\mu_U + 2\mu_O \approx E^{total}_{UO_2} \tag{4}$$

$E^{total}_{UO_2}$ is the total energy per unit formula. Equation (4) is applied at equilibrium. Thus, if one of the chemical potentials becomes critically low, the oxide would decompose into $\alpha$-U and oxygen molecules, which are the reference states used for each element. Therefore, to maintain the oxide form, the range of chemical potentials is limited. When $\alpha$-U begins to form as a result of decomposition, its chemical potential reaches a maximum, which is denoted as the U-rich limit, from the following expression:

$$\mu^{max}_U \approx E^{total}_{\alpha-U} \tag{5}$$

DFT + U was used to calculate the total energy of $E^{total}_{\alpha-U}$ and the value obtained was $-8.48$ eV. According to Formula (4), we can obtain $\mu_O = -10.41$ eV under the U-rich condition.

Because the chemical potentials of U and O atoms are unknown, $\alpha$-U and $O_2$ molecules are considered the reference states, respectively, and combined with

$$\mu^{max}_O \approx \frac{1}{2}E^{total}_{O_2} \tag{6}$$

where the calculated $\frac{1}{2}E^{total}_{O_2}$ is $-4.94$ eV. Hence, we can obtain $\mu_U = -19.41$ eV under O-rich. To study the aggregation behavior of Xe atoms in vacancies, the binding energy ($E_b$) must be calculated. $E_b$ is defined as

$$E_b = E_{n\mathrm{Xe+Vu}} + E^{\mathrm{Int}}_{\mathrm{Xe}} - E_{(n+1)\mathrm{Xe+Vu}} - E_{pri.} \tag{7}$$

where $E_{n\mathrm{Xe+Vu}}$ represents the energy of $n$ Xe atoms on uranium vacancies, $E^{\mathrm{Int}}_{\mathrm{Xe}}$. represents the energy of a Xe atom at the interstitial site, and $E_{(n+1)\mathrm{Xe+Vu}}$ represents the energy of $n + 1$ Xe atoms on uranium vacancies.

## 3. Results and Discussion

### *3.1. Model Verification*

$UO_2$ has a fluorite crystal structure with a space group of $Fm\bar{3}m$. The experimentally measured lattice constant is $a_0 = 5.473$ Å [44]. Figure 1 schematically shows the crystal structure of $UO_2$ with a 1 $k$ AFM configuration.

The ability of DFT + U to accurately calculate the properties of $UO_2$ mainly depends on a valid $U_{eff}$ value ($U_{eff} = U - J$, the difference between the coulomb U and exchange J parameters). Most DFT studies determined to set $U_{eff}$ between 3.0 and 4.0 eV for $UO_2$ through the experimental band gap. It is worth noting that $U_{eff}$ significantly affects the lattice parameters and bulk modulus. This study calculated the corresponding ground state properties of $UO_2$ when $U_{eff}$ was between 3.0 and 4.0 eV and compared them with the experimental values. It was observed that when $U_{eff} = 3.60$ eV, an accurate description of the ground state properties of bulk $UO_2$ could be obtained, as shown in Table 1. Based on this, the finalized occupation matrix control is as follows (the results retain two decimal places):

$$\begin{pmatrix} 0.35 & 0.00 & 0.45 & 0.00 & 0.00 & 0.00 & 0.00 \\ 0.00 & 0.14 & 0.00 & 0.00 & 0.00 & 0.00 & 0.00 \\ 0.45 & 0.00 & 0.67 & 0.00 & 0.00 & 0.00 & 0.00 \\ 0.00 & 0.00 & 0.00 & 0.04 & 0.00 & 0.00 & 0.00 \\ 0.00 & 0.00 & 0.00 & 0.00 & 0.67 & 0.00 & -0.45 \\ 0.00 & 0.00 & 0.00 & 0.00 & 0.00 & 0.03 & 0.00 \\ 0.00 & 0.00 & 0.00 & 0.00 & -0.45 & 0.00 & 0.35 \end{pmatrix}$$

**Table 1.** Lattice parameter ($a_0$), band gap ($E_{gap}$), magnetic moment ($\mu_B$), bulk modulus ($B_0$), and cohesive energy ($E_{coh}$) of the $UO_2$ at the ground state, compared to the reported experimental values (Exp.).

| Method | $a_0$ (Å) | $E_{gap}$ (eV) | $\mu_B$ | $B_0$ (GPa) | $E_{coh}$ (eV/$UO_2$) |
|---|---|---|---|---|---|
| DFT + U [45] | 5.475 | 2.13 | 2.01 | 213 | - |
| LDA + U [46] | 5.474 | 2.06 | 1.35 | 210 | - |
| GGA + U [47] | 5.52 | 1.8 | 1.94 | 209 | −21.7 |
| GGA + U [a] | 5.497 | 2.14 | 1.99 | 207.2 | −22.3 |
| Exp. | 5.473 [44] | 2.1 [48] | 1.74 [49] | 209 [50] | −22.0 [51] |

[a] This work.

This is consistent with the occupation matrix for the ground state of $UO_2$ determined by Dorado et al. [34] and Torres et al. [45]. This shows that the OMC scheme has good repeatability for investigating $UO_2$.

As shown in Table 1, the ground state properties of $UO_2$ were calculated and compared with the previously reported theoretical and experimental results. Using the OMC scheme, the lattice parameter was 5.497 Å, band gap was 2.14 eV, bulk modulus was 207.2 GPa, and cohesive energy was −22.3 eV. The results for the band gap, magnetic moment, and bulk modulus are consistent with those obtained by Torres et al. [45]. However, the lattice parameters were slightly larger by 0.4% compared with the that of the literature data (5.475 Å) and the experimental data (5.473 Å). This is mainly because of the use of PBEsol functional calculations in the literature. Moreover, we did not find a significant relationship between the $U_{eff}$ value and the size of the magnetic moment, which also confirms that the ground state occupation matrix could ensure the accurate calculation of the nature of the ground state of $UO_2$. In this study, we calculated the ground state of the elastic constants and elastic modulus of $UO_2$ and the elastic modulus of components $C_{11}$ = 378.6, $C_{12}$ = 118.0, and $C_{44}$ = 67.2 GPa, and experimental data [50] were $C_{11}$ = 389.3, $C_{12}$ = 118.7, and $C_{44}$ = 59.7 GPa, respectively. This shows that the calculated values are in good agreement with the experimental values.

### *3.2. Th, Zr, and Ti Dopants in $UO_2$*

Th, Zr, and Ti are the main metallic fission products in $UO_2$ fuel. These dopants usually occupy the U sites because of their similar electronegativities and radii [52]. In this study, only one U atom was replaced by a dopant, and the doping concentration was 3.125 atm %. Ti, Th, and Zr were also calculated using the DFT + U method. $U_{eff}$ was determined by calculating the ground state properties of $ThO_2$, $ZrO_2$, and $TiO_2$. The corresponding values were 0.0, 4.0, and 4.0 eV respectively (Tables S1–S3). Table 2 lists the energy properties obtained by substituting U atoms with dopants Th, Zr, and Ti in the 2 × 2 × 2 supercells of $UO_2$. According to the calculation results, the incorporation energy of Th replacing the U atom is −10.25 eV, which is 4.56 eV lower than that of Ti. The solution energy of Th on the U vacancy is also lower than that of Ti. The incorporation energy and solution energy of Zr substituted for U atoms were between those of Th and Ti. The results show that Th is easier to dissolve in U vacancies than Zr or Ti. In particular, in the O-rich state, the solution energy of dopants Th, Zr, and Ti on the U vacancy is much lower than in the U-rich state.

This is because with the continuous nuclear reaction, the U atom is continuously consumed, and the formation energy of U vacancy is continuously reduced, resulting in such a result.

**Table 2.** Energy properties obtained by substituting U atoms with dopants Th, Zr, and Ti in 2 × 2 × 2 supercells of $UO_2$.

| Materials | Incorporation Energy (eV) | Solution Energy (eV) | |
|---|---|---|---|
| | | O-Rich | U-Rich |
| $UO_2$-Th | −10.25 | −11.76 | −0.83 |
| $UO_2$-Zr | −8.68 | −10.19 | 0.74 |
| $UO_2$-Ti | −5.69 | −7.2 | 3.73 |

Figure 2 shows the electron charge densities of pure $UO_2$ and Th, Zr, and Ti replacing U-defect $UO_2$. It can be observed from the figure that the interaction of the Th-O bond is similar to that of the U-O bond in pure $UO_2$. The interaction of the Ti-O bond is the weakest, and Ti is almost isolated in the uranium vacancy. The strength of the Zr-O bond is between that of the Th-O and Ti-O bonds, which also corresponds to the calculated dissolution energy data. Table 3 shows the Bader charges of pure $UO_2$, and the Th-, Zr-, and Ti-substituted U-defect $UO_2$ systems. In pure $UO_2$, the Bader charge of U atom and the nearest neighbor O atom is 2.50 and −1.25 |e|, respectively. The Bader charge of the nearest neighbor O atom around Th increases by 0.05 |e|, and that of the nearest neighbor O atom around Zr increases by 0.06 |e|. This indicates that the Th and Zr atomic orbitals have more delocalized features than the U atomic orbitals.

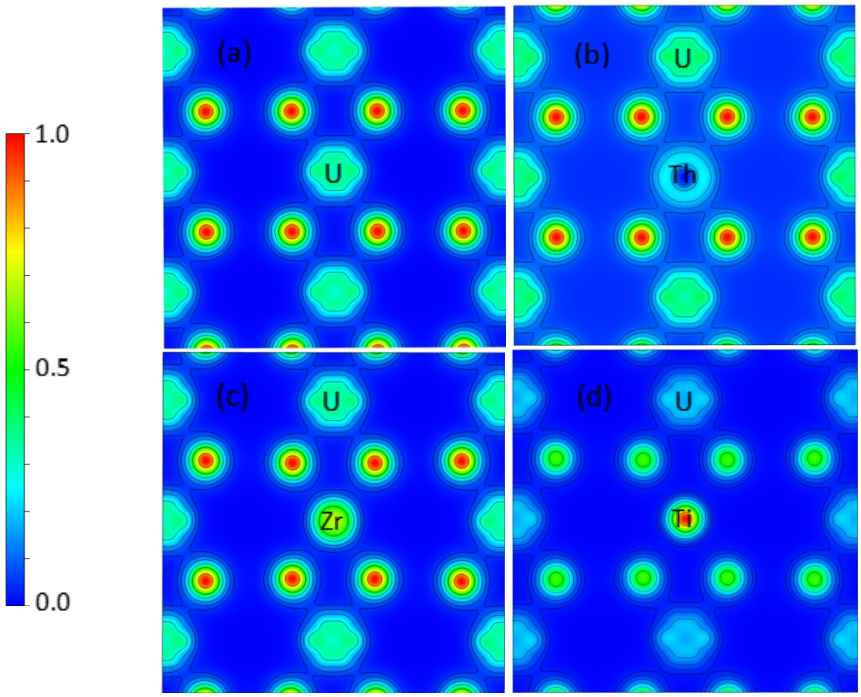


**Figure 2.** Electron charge density contour plots of $UO_2$ in the $z = 0$ plane, (**a**) U atom in perfect $UO_2$, (**b**) Th-doped $UO_2$, (**c**) Zr-doped $UO_2$, and (**d**) Ti-doped $UO_2$.

**Table 3.** Atomic Bader charges ( | e | ) of pure $UO_2$, and Th, Zr, and Ti substituted U defect $UO_2$ system.

| Materials | Centre Atom | Nearest O Atom | Nearest U Atom |
|---|---|---|---|
| $UO_2$ | 2.50 (U) | −1.25 | 2.50 |
| $UO_2$-Th | 2.64 (Th) | −1.30 | 2.51 |
| $UO_2$-Zr | 2.48 (Zr) | −1.31 | 2.57 |
| $UO_2$-Ti | 2.09 (Ti) | −1.28 | 2.57 |

Next, we discuss Th-, Zr-, and Ti-doped $U_{32}O_{64}$ systems. The changes in the unit lattice volume and bond length of all systems were calculated and are provided in Table 4. The lattice volume and bond length changed with the different dopants. The incorporation of Th caused the lattice volume to expand by 0.16% and increased the bond length of Th-O by 0.65%. However, the incorporation of Zr and Ti caused the lattice volume to shrink by 0.52% and 0.88%, respectively. The lattice distortion can be attributed to the radius difference between the dopant and $U^{4+}$ ions. The ionic radius of $Th^{4+}$ was slightly larger than that of $U^{4+}$, whereas the ionic radii of $Zr^{4+}$ and $Ti^{4+}$ were smaller than those of $U^{4+}$. Therefore, the relative change rate of the dopant system in Table 4 is reasonable.

**Table 4.** Relative changes in lattice volume and bond length. X-U and X-O denote the distance between dopant and nearest uranium atom and oxygen atom, respectively. U-U denotes the distance between uranium atoms, U-O represents the distance between uranium atom and oxygen atom, and Δ (X-U) and Δ (X-O) is the absolute change in bond length. Absolute variation of complete $UO_2$ volume ($V_0$) and doped $UO_2$ volume (ΔV).

| Materials | Δ (X-U)/U-U | Δ (X-O)/U-O | $\Delta V/V_0$ |
|---|---|---|---|
| $UO_2$-Th | 0.15% | 0.65% | 0.16% |
| $UO_2$-Zr | −0.79% | −3.85% | −0.52% |
| $UO_2$-Ti | −1.33% | −2.78% | −0.88% |

### *3.3. Effect of Dopant on Xe in $UO_2$*

To investigate the influence of the dopants on Xe, the incorporation energy required for Xe absorption on the vacancy defect was calculated, and the results are shown in Figure 3. In the $UO_2$ system, Xe was more readily adsorbed onto the SD1 defects. The corresponding incorporation energy was 1.22 eV, indicating that Xe is easily captured by neutral three-vacancies. This is consistent with the experimental data [53]. It is difficult for Xe to exist in the interstitial sites. Although the Ti dopant can significantly reduce the incorporation energy of Xe, its incorporation energy is as high as 6.47 eV. This suggests that Xe atoms are more likely to bind in the larger space of the vacancy defect pores because of their large radius and inability to bond with surrounding atoms. In various doping systems, the dopants have different effects on the incorporation energy of Xe in different vacancy defects.

For Di and SD defects, the presence of dopants increases the incorporation energy required by Xe, whereas for other simple defects, the existence of dopants reduces the incorporation energy of Xe atoms. This implies that the incorporation energy of Xe on the vacancy is not only related to the volume of the vacancy defect but also to the complex situation around the defect. Compared with other dopants, the Ti atom has the greatest influence on the binding energy of the Xe atom in the Int and Vo defects, and this can significantly reduce the binding energy. This implies that when vacancies are pre-existing, for instance, under irradiation conditions, the Ti atom has a favored function to form a combination of Xe and vacancies.

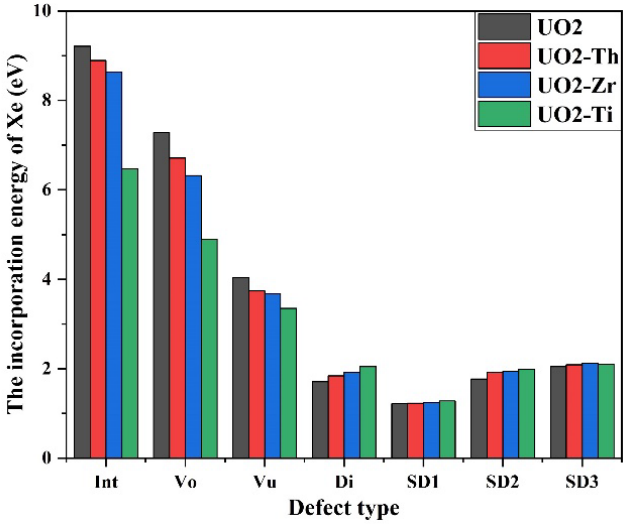


**Figure 3.** Incorporation energy of Xe at different defect type positions and the effect of dopant on its incorporation energy.

To determine the influence of dopants in $UO_2$ on the dissolution ability of Xe, we added the formation energy of vacancy defects and incorporation energy of Xe absorption to obtain the solution energy of Xe. The calculation results are shown in Figure 4. In U-rich samples, the lowest solution energy of Xe atoms in SD2 defects in pure $UO_2$ is 3.74 eV, and the highest solution energy is in uranium vacancies. Under O-rich conditions, the solution energy of the Xe atom in the oxygen vacancy is the highest, and it is easily dissolved in the uranium–oxygen dual vacancy, which is consistent with the results reported by Bés et al. [54]. This indicates that in the actual reactor, the dissolution ability of Xe in the $UO_2$ vacancy defect also changes as the reaction progresses. In various doping systems, the presence of dopants reduces the solution energy of Xe in various defects. Under the same configuration, the $UO_2$-Th system has the lowest influence on the dissolution energy of the Xe atom, that is, it can only slightly reduce the dissolution energy. This is because the ionic radii of $Th^{4+}$ and $U^{4+}$ are 1.09 and 1.0 Å, and the difference between the ionic radii is small. The electronegativity of U atoms is slightly stronger than that of Th atoms. In the periodic table of elements, they are located close to each other and belong to the actinide series. Additionally, the interaction strength between U-O bonds is similar to Th-O bonds. Therefore, the doping of Th has minimal effect on the structure in $UO_2$. The $UO_2$-Ti system has a significant influence on the solubility of Xe. Specifically, it can reduce the solubility energy of Xe on all vacancies. The reason is that the electronegativity of the Ti atom is slightly stronger than that of the U atom, its ability to attract electrons is stronger, and the ionic radius of $Ti^{4+}$ is much smaller than that of $U^{4+}$. Therefore, the interaction between Ti atoms and the surrounding O atoms was substantially weak, providing a favorable space for the dissolution of Xe atoms. The effect of the $UO_2$-Zr system on the solubility energy of the Xe atom was intermediate. This is because the electronegativity or ionic radius, $Zr^{4+}$ ions are between $Th^{4+}$ and $Ti^{4+}$ ions. In particular, for the $UO_2$-Ti system in the U-rich condition, the solubility energy of Xe in oxygen vacancies was significantly reduced. It was also the lowest among all the calculated defects, with a value of only 1.86 eV. This indicates that Xe atoms tend to dissolve near the oxygen vacancy around Ti at the initial stage of nuclear fuel. This consequently expands the volume of $UO_2$ by approximately 1.7% at the initial stage of the reaction. Therefore, the doping agent Ti has the most apparent effect on the Xe space.

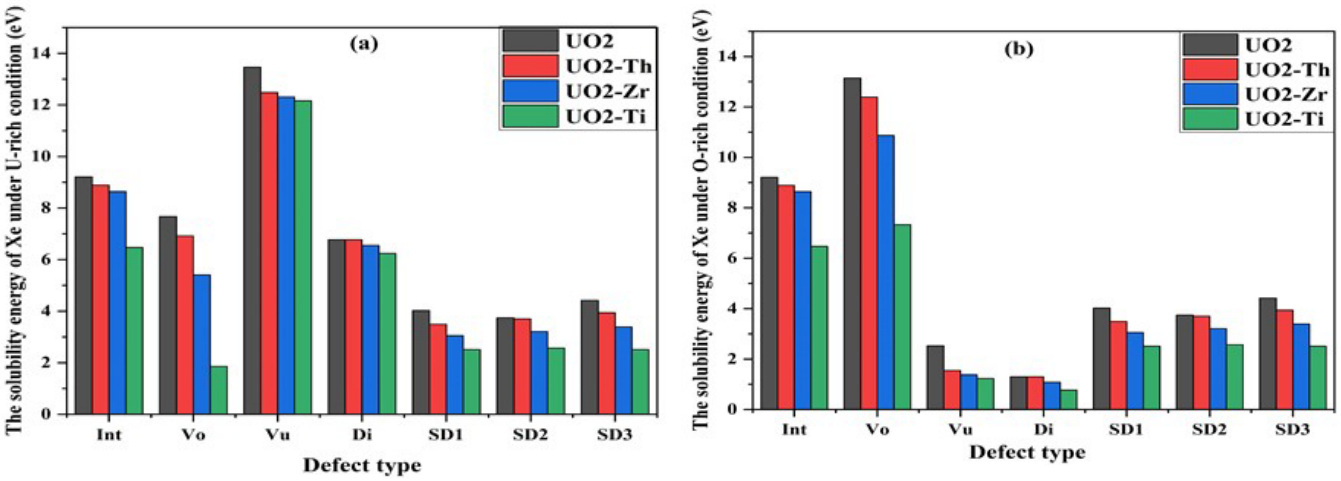


**Figure 4.** (**a**) Under the U-rich condition, the solution energy of Xe at different defect locations and the influence of dopants on it. (**b**) Under the Os-rich condition, the solution energy of Xe at different defect locations and the influence of dopants on it.

In the final stage of the $UO_2$ reaction, more vacancies are generated in the lattice under irradiation conditions, which is the main factor for the nucleation and growth of Xe atoms. Therefore, it is necessary to investigate the aggregation behavior of Xe atoms and the influence of dopants Th, Zr, and Ti on such behavior, when the dopant is located at the nearest position to the vacancy defect. The above results show that under O-rich conditions, Xe atoms are more likely to occupy uranium vacancies; therefore, we studied the aggregation behavior of Xe on uranium vacancies. The binding energies of the Xe atoms on the vacancies that we calculated using Equation (7) are shown in Table 5. It can be observed that the binding energy of Xe atoms varies with the number of atoms in both pure $UO_2$ and doped systems. This implies that the stability of Xe clusters is closely related to their numbers. In a pure $UO_2$ system, an Xe atom is easily bound to a uranium vacancy to form a Xe-Vu complex. When the second Xe atom is added to the nearest interstitial site of the Xe-Vu complex (Figure 5, $V_{Int1}$), the binding energy becomes 1.96 eV. This indicates that the Xe-Vu complex can absorb another Xe atom to form a 2Xe-Vu complex. When the third Xe atom is located in the nearest gap position of the 2Xe-Vu complex (Figure 5, $V_{Int2}$), a 3Xe-Vu complex structure is formed, with a binding energy of 3.11 eV, indicating that the cluster effect is more obvious with the increase in the *n*Xe-Vu cluster size. To better explain this result, the influence of the space volume of the gap position was analyzed, as shown in Figure 5 and Table 6. It can be observed from Table 6 that in pure $UO_2$, the volume of the gap is 21.26 $Å^3$. When Xe binds to a uranium vacancy to form a Xe-Vu complex, the volume expansion of the nearest interstitial site is 22.47 $Å^3$. After two Xe atoms combine with $UO_2$ to form a 2Xe-Vu complex, $V_{Int2}$ increases to 26.39 $Å^3$, creating sufficient space for the combination of the third Xe atom. Therefore, when the third Xe atom combines with the $V_{Int2}$ interstitial site, the binding energy increases.

**Table 5.** Relationship between binding energy (eV) and number of Xe atoms in pure $UO_2$, $UO_2$-Th, $UO_2$-Zr, and $UO_2$-Ti systems.

| Materials | $UO_2$ | $UO_2$-Th | $UO_2$-Zr | $UO_2$-Ti |
|---|---|---|---|---|
| $Xe_1$ | 5.17 | 5.12 | 4.96 | 3.12 |
| $Xe_2$ | 1.96 | 1.60 | 1.47 | 1.17 |
| $Xe_3$ | 3.11 | 2.68 | 2.22 | 0.89 |

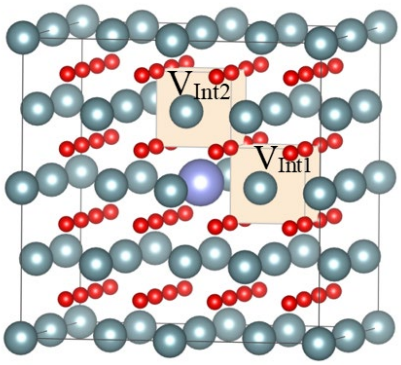


**Figure 5.** Cluster behavior of Xe atoms in pure $UO_2$. Red sphere, grey sphere, and blue sphere represent oxygen atom, uranium atom, and Xe atom, respectively. Yellow represents the volume of the interstitial site.

**Table 6.** Cluster behavior of Xe atoms in pure $UO_2$ results in a volume change of interstitial sites.

| Materials | $V_{Int1}$ (Å$^3$) | $V_{Int2}$ (Å$^3$) |
|---|---|---|
| $UO_2$ | 21.26 | 21.26 |
| $UO_2$-$Xe_1$ | 22.47 | 22.47 |
| $UO_2$-$Xe_2$ | - | 26.39 |

As shown in Table 5, the addition of dopants weakens the aggregation of Xe in the vacancy. In the $UO_2$-Th system, Xe atoms combine with vacancies to form a Xe-Vu complex and *n*Xe-Vu complexes. The binding energy decreases to some extent, indicating that Th weakens the aggregation behavior of Xe atoms. In the $UO_2$-Ti system, the binding energy of a Xe atom from the interstitial site into the uranium vacancy is 3.12 eV, which is 2.05 eV lower than that of pure $UO_2$. The binding energy required for multiple Xe to form *n*Xe-Vu complexes is also much lower than that of pure $UO_2$. Apparently, Ti significantly weakens the aggregation behavior of Xe atoms. This is because Ti doping will greatly reduce the binding energy of Xe at the interstitial site, thereby reducing the ability of Xe to migrate from the interstitial site to the uranium vacancy, making it difficult for Xe to aggregate near the uranium vacancy. In the $UO_2$-Zr system, Zr also weakens the aggregation behavior of Xe on uranium vacancies. The effect of Zr on the binding energy of Xe on the interstitial and uranium vacancies is moderate, between that of Th and Ti.

## 4. Conclusions

The crystal model of $UO_2$ was verified by the DFT + U method, and the $U_{eff}$ value was determined. The OMC scheme is adopted to ensure that the subsequent calculation of the defect system can converge to the ground state. The calculation method in this paper makes the ground state properties of $UO_2$ showed significant improvement compared with existing theoretical results and was consistent with experimental data. This study set out to investigate the influence of Th, Zr, and Ti dopants on the solution property of Xe in $UO_2$ with defects. The incorporation energy results shows that impurity atoms allow Xe atoms to incorporate easily into simple vacancy defects. The solution energy results show that dopants Th, Zr, and Ti atoms can all promote the dissolution of Xe atoms in vacancy defects. Among them, Ti atoms are most conducive to the dissolution of Xe atoms into defects due to their small atomic radii and large electronegativity. By studying the aggregation behavior of Xe at the vacancies, it was observed that $UO_2$ promoted the formation of a 3Xe-Vu complex. However, dopant addition reduces the binding energy of Xe at interstitial sites, thereby reducing the ability of Xe to migrate from interstitial sites to uranium vacancies, making it difficult for Xe atoms to nucleate and grow. In addition, Ti is the least conducive to the aggregation of Xe clusters. The experimental scheme and results of this study will provide useful guidance for the simulation and experiment of nuclear fuel in the future.

**Supplementary Materials:** The following supporting information can be downloaded at: https://www.mdpi.com/article/10.3390/met12050879/s1, Table S1: Ground state properties of $ThO_2$ under different $U_{eff}$ values. Lattice parameter (a, b, c), band gap ($E_{gap}$), bulk modulus (B), shear modulus(G), Young's modulus(E), elastic constant ($C_{11}$, $C_{12}$, $C_{44}$), compared to the reported experimental values (Exp.); Table S2: Ground state properties of $ZrO_2$ under different $U_{eff}$ values. Lattice parameter (a, b, c), band gap ($E_{gap}$), bulk modulus (B), shear modulus(G), Young's modulus(E), elastic constant ($C_{11}$, $C_{12}$, $C_{33}$, $C_{44}$, $C_{66}$), compared to the reported experimental values (Exp.); Table S3: Ground state properties of $TiO_2$ under different $U_{eff}$ values. Lattice parameter (a, b, c), band gap ($E_{gap}$), bulk modulus (B), shear modulus(G), Young's modulus(E), elastic constant ($C_{11}$, $C_{12}$, $C_{13}$, $C_{33}$, $C_{44}$, $C_{66}$), compared to the reported experimental values (Exp.). References [54–72] are cited in the Supplementary Materials.

**Author Contributions:** Modeling construction and simulation, data collection, data analysis, writing the original draft, L.P.; study design, result discussion, editing the manuscript, Z.W.; result discussion, editing the manuscript, Q.W.; study design, result discussion, editing the manuscript, Z.L.; editing the manuscript, M.P.; study design, editing the manuscript, Z.H.; result discussion, editing the manuscript, L.W. All authors have read and agreed to the published version of the manuscript.

**Funding:** This research received no external funding.

**Institutional Review Board Statement:** Not applicable.

**Informed Consent Statement:** Not applicable.

**Data Availability Statement:** Data sharing is not applicable.

**Conflicts of Interest:** The authors declare no conflict of interest.

## References

1. Zhang, Y.-J.; Lan, J.-H.; Wang, C.-Z.; Wu, Q.-Y.; Bo, T.; Chai, Z.-F.; Shi, W.-Q. Theoretical Investigation on Incorporation and Diffusion Properties of Xe in Uranium Mononitride. *J. Phys. Chem. C* **2015**, *119*, 5783–5789. [CrossRef]
2. Andersson, A.D.; Perriot, R.T.; Pastore, G.; Tonks, M.R.; Cooper, M.W.; Liu, X.-Y.; Goyal, A.; Uberuaga, B.P.; Stanek, C.R. *Report on Simulation of Fission Gas and Fission Product Diffusion in Uo$_2$*; Los Alamos National Lab.: Los Alamos, NM, USA, 2016. [CrossRef]
3. White, R.J.; Tucker, M.O. A new fission-gas release model. *J. Nucl. Mater.* **1983**, *118*, 1–38. [CrossRef]
4. White, R.J. The development of grain-face porosity in irradiated oxide fuel. *J. Nucl. Mater.* **2004**, *325*, 61–77. [CrossRef]
5. B.RT.Frost. Volumes 10A and 10B of Materials science and technology–A Comprehensive treatment. *Adv. Mater.* **1995**, *7*, 1047. [CrossRef]
6. Zinkle, S.J.; Was, G.S. Materials challenges in nuclear energy. *Acta Mater.* **2013**, *61*, 735–758. [CrossRef]
7. Pang, J.W.L.; Chernatynskiy, A.; Larson, B.C.; Buyers, W.J.L.; Abernathy, D.L.; McClellan, K.J.; Phillpot, S.R. Phonon density of states and anharmonicity of $UO_2$. *Phys. Rev. B* **2014**, *89*, 115132. [CrossRef]
8. Ao, B.; Lu, H. First-principles energetics of rare gases incorporation into uranium dioxide. *Phys. Rev. B* **2016**, *373*, 102–109. [CrossRef]
9. Une, K.; Tanabe, I.; Oguma, M. Effects of additives and the oxygen potential on the fission gas diffusion in $UO_2$ fuel. *J. Nucl. Mater.* **1987**, *150*, 93–99. [CrossRef]
10. Fujino, T.; Shiratori, T.; Sato, N.; Fukuda, K.; Yamada, K.; Serizawa, H. Post-irradiation examination of high burnup Mg doped $UO_2$ in comparison with undoped $UO_2$, Mg–Nb doped $UO_2$ and Ti doped $UO_2$. *J. Nucl. Mater.* **2001**, *297*, 176–205. [CrossRef]
11. Fujino, T.; Nakama, S.; Sato, N.; Yamada, K.; Fukuda, K.; Serizawa, H.; Shiratori, T. Solubility of magnesium in uranium dioxide. *J. Nucl. Mater.* **1997**, *246*, 150–157. [CrossRef]
12. Kashibe, S.; Une, K. Effect of additives ($Cr_2O_3$, $Al_2O_3$, $SiO_2$, MgO) on diffusional release of 133Xe from $UO_2$ fuels. *J. Nucl. Mater.* **1998**, *254*, 234–242. [CrossRef]
13. Matsui, T.; Arita, Y.; Naito, K. High temperature heat capacities and electrical conductivities of $UO_2$ doped with Ti, Nb and Sc. *Solid State Ion.* **1991**, *49*, 195–200. [CrossRef]
14. Aybers, M.T.; Artir, R.; Akşit, A.A.; Akbal, S. Investigation of some mechanical properties of $Ti_2O_3$-doped $UO_2$ fuel pellets. *Mater. Charact.* **2006**, *57*, 182–186. [CrossRef]
15. Peres, V.; Favergeon, L.; Andrieu, M.; Palussière, J.C.; Balland, J.; Delafoy, C.; Pijolat, M. High temperature chromium volatilization from $Cr_2O_3$ powder and $Cr_2O_3$-doped $UO_2$ pellets in reducing atmospheres. *J. Nucl. Mater.* **2012**, *423*, 93–101. [CrossRef]
16. Yang, J.; Shen, L.; Yang, G.-W.; Li, Q.-Y.; Zhu, L.-L.; Shen, W.; Ji, C.; Shen, X.-F. Four novel coordination compounds containing Hpypza ligand [Hpypza=[3-(2-pyridyl)-1-pyrazolyl] acetic acid]. *Inorg. Chim. Acta* **2012**, *392*, 25–29. [CrossRef]
17. Cohen, I.; Schaner, B.E. A metallographic and X-ray study of the $UO_2$-$ZrO_2$ system. *J. Nucl. Mater.* **1963**, *9*, 18–52. [CrossRef]
18. Kulkarni, N.K.; Krishnan, K.; Kasar, U.M.; Rakshit, S.K.; Sali, S.K.; Aggarwal, S.K. Thermal studies on fluorite type $Zr_yU_{1-y}O_2$ solid solutions. *J. Nucl. Mater.* **2009**, *384*, 81–86. [CrossRef]

19. Xiao, H.; Long, C.; Chen, H.; Tian, X.; Wei, T.; Zhao, Y.; Gao, W. Effects of Zr doping on the surface energy and surface structure of $UO_2$: Atomistic simulations. *Appl. Surf. Sci.* **2015**, *351*, 517–523. [CrossRef]
20. Ang, C.Y.; Burkhammer, K.W. Sintering of high density uranium dioxide bodies. *J. Nucl. Mater.* **1960**, *2*, 176–180. [CrossRef]
21. Rickert, K.; Prusnick, T.A.; Hunt, E.; Kimani, M.M.; Chastang, S.; Brooks, D.L.; Moore, E.A.; Petrosky, J.C.; Mann, J.M. Inhibiting laser oxidation of $UO_2$ via Th substitution. *J. Nucl. Mater.* **2019**, *517*, 254–262. [CrossRef]
22. Sholl, D.; Steckel, J.A. *Density Functional Theory: A Practical Introduction*; John Wiley & Sons: New York, NY, USA, 2011.
23. Hohenberg, P.; Kohn, W. Density functional theory (DFT). *Phys. Rev.* **1964**, *136*, B864. [CrossRef]
24. Ao, B.; Qiu, R.; Zhang, G.; Pu, Z.; Wang, X.; Shi, P. Light impurity atoms as the probes for the electronic structures of actinide dioxides. *Comput. Mater. Sci.* **2018**, *142*, 25–31. [CrossRef]
25. Van Brutzel, L.; Rarivomanantsoa, M. Molecular dynamics simulation study of primary damage in $UO_2$ produced by cascade overlaps. *J. Nucl. Mater.* **2006**, *358*, 209–216. [CrossRef]
26. Martin, G.; Garcia, P.; Van Brutzel, L.; Dorado, B.; Maillard, S. Effect of the cascade energy on defect production in uranium dioxide. *Nucl. Instrum. Methods Phys. Res. Sect. B Beam Interact. Mater. At.* **2011**, *269*, 1727–1730. [CrossRef]
27. Yu, J.; Devanathan, R.; Weber, W.J. First-principles study of defects and phase transition in $UO_2$. *J. Phys. Condens. Matter* **2009**, *21*, 435401. [CrossRef]
28. Nerikar, P.; Watanabe, T.; Tulenko, J.S.; Phillpot, S.R.; Sinnott, S.B. Energetics of intrinsic point defects in uranium dioxide from electronic-structure calculations. *J. Nucl. Mater.* **2009**, *384*, 61–69. [CrossRef]
29. Kresse, G.; Furthmüller, J. Efficient iterative schemes for ab initio total-energy calculations using a plane-wave basis set. *Phys. Rev. B* **1996**, *54*, 11169–11186. [CrossRef]
30. Blöchl, P.E. Projector augmented-wave method. *Phys. Rev. B* **1994**, *50*, 17953–17979. [CrossRef]
31. Kresse, G.; Joubert, D. From ultrasoft pseudopotentials to the projector augmented-wave method. *Phys. Rev. B* **1999**, *59*, 1758–1775. [CrossRef]
32. Perdew, J.P.; Burke, K.; Ernzerhof, M. Generalized Gradient Approximation Made Simple. *Phys. Rev. Lett.* **1996**, *77*, 3865–3868. [CrossRef]
33. Monkhorst, H.J.; Pack, J.D. Special points for Brillouin-zone integrations. *Phys. Rev. B* **1976**, *13*, 5188–5192. [CrossRef]
34. Dorado, B.; Freyss, M.; Amadon, B.; Bertolus, M.; Jomard, G.; Garcia, P. Advances in first-principles modelling of point defects in $UO_2$: f electron correlations and the issue of local energy minima. *J. Phys. Condens. Matter* **2013**, *25*, 333201. [CrossRef] [PubMed]
35. Jollet, F.; Petit, T.; Gota, S.; Thromat, N.; Gautier-Soyer, M.; Pasturel, A. The electronic structure of uranium dioxide: An oxygen K-edge X-ray absorption study. *J. Phys. Condens. Matter* **1997**, *9*, 9393–9401. [CrossRef]
36. Crocombette, J.P.; Jollet, F.; Nga, L.T.; Petit, T. Plane-wave pseudopotential study of point defects in uranium dioxide. *Phys. Rev. B* **2001**, *64*, 104107. [CrossRef]
37. Freyss, M.; Petit, T.; Crocombette, J.-P. Point defects in uranium dioxide: Ab initio pseudopotential approach in the generalized gradient approximation. *J. Nucl. Mater.* **2005**, *347*, 44–51. [CrossRef]
38. Dudarev, S.L.; Botton, G.A.; Savrasov, S.Y.; Humphreys, C.J.; Sutton, A.P. Electron-energy-loss spectra and the structural stability of nickel oxide: An LSDA+U study. *Phys. Rev. B* **1998**, *57*, 1505–1509. [CrossRef]
39. Dudarev, S.L.; Castell, M.R.; Botton, G.A.; Savrasov, S.Y.; Muggelberg, C.; Briggs, G.A.D.; Sutton, A.P.; Goddard, D.T. Understanding STM images and EELS spectra of oxides with strongly correlated electrons: A comparison of nickel and uranium oxides. *Micron* **2000**, *31*, 363–372. [CrossRef]
40. Dorado, B.; Amadon, B.; Freyss, M.; Bertolus, M. DFT+U calculations of the ground state and metastable states of uranium dioxide. *Phys. Rev. B* **2009**, *79*, 235125. [CrossRef]
41. Solomon, J.M.; Alexandrov, V.; Sadigh, B.; Navrotsky, A.; Asta, M. Computational study of the energetics and defect clustering tendencies for Y- and La-doped $UO_2$. *Acta Mater.* **2014**, *78*, 282–289. [CrossRef]
42. Dorado, B.; Jomard, G.; Freyss, M.; Bertolus, M. Stability of oxygen point defects in $UO_2$ by first-principles DFT+U calculations: Occupation matrix control and Jahn-Teller distortion. *Phys. Rev. B* **2010**, *82*, 035114. [CrossRef]
43. Grimes, R.W.; Catlow, C.R.A. The stability of fission products in uranium dioxide. *Philos. Trans. R. Soc. London. Ser. A Phys. Eng. Sci.* **1991**, *335*, 609–634. [CrossRef]
44. Idiri, M.; Le Bihan, T.; Heathman, S.; Rebizant, J. Behavior of actinide dioxides under pressure: $UO_2$ and $ThO_2$. *Phys. Rev. B* **2004**, *70*. [CrossRef]
45. Torres, E.; Kaloni, T.P. Thermal conductivity and diffusion mechanisms of noble gases in uranium dioxide: A DFT+U study. *J. Nucl. Mater.* **2019**, *521*, 137–145. [CrossRef]
46. Pegg, J.T.; Aparicio-Anglès, X.; Storr, M.; de Leeuw, N.H. DFT+U study of the structures and properties of the actinide dioxides. *J. Nucl. Mater.* **2017**, *492*, 269–278. [CrossRef]
47. Gupta, F.; Brillant, G.; Pasturel, A. Correlation effects and energetics of point defects in uranium dioxide: A first principle investigation. *Philos. Mag.* **2007**, *87*, 2561–2569. [CrossRef]
48. Yu, S.-W.; Tobin, J.G.; Crowhurst, J.C.; Sharma, S.; Dewhurst, J.K.; Velasco, P.O.; Yang, W.L.; Siekhaus, W.J. f-f origin of the insulating state in uranium dioxide: X-ray absorption experiments and first-principles calculations. *Phys. Rev. B* **2011**, *83*, 165102. [CrossRef]
49. Faber, J.; Lander, G.H. Neutron diffraction study of $UO_2$: Antiferromagnetic state. *Phys. Rev. B* **1976**, *14*, 1151–1164. [CrossRef]
50. Fritz, I.J. Elastic properties of $UO_2$ at high pressure. *J. Appl. Phys.* **1976**, *47*, 4353–4358. [CrossRef]

51. Brooks, M.S.S.; Kelly, P.J. On the cohesive energy and charge density of uranium dioxide. *Solid State Commun.* **1983**, *45*, 689–692. [CrossRef]
52. Lan, J.-H.; Wang, L.; Li, S.; Yuan, L.-Y.; Feng, Y.-X.; Sun, W.; Zhao, Y.-L.; Chai, Z.-F.; Shi, W.-Q. First principles modeling of zirconium solution in bulk $UO_2$. *J. Appl. Phys.* **2013**, *113*, 183514. [CrossRef]
53. Matzke, H.J. Gas release mechanisms in $UO_2$—A critical review. *Radiat. Eff.* **1980**, *53*, 219–242. [CrossRef]
54. Bès, R.; Martin, P.; Vathonne, E.; Delorme, R.; Sabathier, C.; Freyss, M.; Bertolus, M.; Glatzel, P. Experimental evidence of Xe incorporation in Schottky defects in $UO_2$. *Appl. Phys. Lett.* **2015**, *106*, 114102. [CrossRef]
55. Griffiths, T.R.; Dixon, J. Electron irradiation of single crystal thorium dioxide and electron transfer reactions. *Inorg. Chim. Acta* **2000**, *300–302*, 305–313. [CrossRef]
56. Shields, A.; Santos-Carballal, D.; de Leeuw, N.H. A density functional theory study of uranium-doped thoria and uranium adatoms on the major surfaces of thorium dioxide. *J. Nucl. Mater.* **2016**, *473*, 99–111. [CrossRef]
57. Delarmelina, M.; Quesne, M.G.; Catlow, C.R.A. Modelling the bulk properties of ambient pressure polymorphs of zirconia. *Phys. Chem. Chem. Phys.* **2020**, *22*, 6660–6676. [CrossRef] [PubMed]
58. Stausholm-Møller, J.; Kristoffersen, H.H.; Hinnemann, B.; Madsen, G.K.; Hammer, B. DFT+ U study of defects in bulk rutile $TiO_2$. *J. Chem. Phys.* **2010**, *133*, 144708. [CrossRef] [PubMed]
59. Morgan, B.J.; Watson, G.W. Intrinsic n-type Defect Formation in TiO2: A Comparison of Rutile and Anatase from GGA+U Calculations. *J. Phys. Chem. C* **2010**, *114*, 2321–2328. [CrossRef]
60. Morgan, B.; Watson, G. A DFT+U description of oxygen vacancies at the TiO2 rutile (110) surface. *Surf. Sci.* **2007**, *601*, 5034–5041. [CrossRef]
61. Prada, S.; Rosa, M.; Giordano, L.; Di Valentin, C.; Pacchioni, G. Density functional theory study of TiO2/Ag interfaces and their role in memristor devices. *Phys. Rev. B* **2011**, *83*. [CrossRef]
62. Morgan, B.J.; Madden, P.A. Lithium intercalation into TiO2(B): A comparison of LDA, GGA, and GGA+Udensity functional calculations. *Phys. Rev. B* **2012**, *86*. [CrossRef]
63. Olsen, J.S.; Gerward, L.; Kanchana, V.; Vaitheeswaran, G. The bulk modulus of ThO2—an experimental and theoretical study. *J. Alloy. Compd.* **2004**, *381*, 37–40. [CrossRef]
64. Idiri, M.; Le Bihan, T.; Heathman, S.; Rebizant, J. Behavior of actinide dioxides under pressure: UO22 and ThO2. *Phys. Rev. B* **2004**, *70*, 014113. [CrossRef]
65. Macedo, P.; Capps, W.; Wachtman Jr, J. Elastic constants of single crystal ThO2 at 25 °C. *J. Am. Ceram. Soc.* **1964**, *47*, 651–651. [CrossRef]
66. Stefanovich, E.; Shluger, A.L.; Catlow, C. Theoretical study of the stabilization of cubic-phase $ZrO_2$ by impurities. *Phys. Rev. B* **1994**, *49*, 11560. [CrossRef] [PubMed]
67. Chan, S.-K.; Fang, Y.; Grimsditch, M.; Li, Z.; Nevitt, M.V.; Robertson, W.M.; Zouboulis, E.S. Temperature Dependence of the Elastic Moduli of Monoclinic Zirconia. *J. Am. Ceram. Soc.* **1991**, *74*, 1742–1744. [CrossRef]
68. Nevitt, M.; Chan, S.-K.; Liu, J.; Grimsditch, M.; Fang, Y. The elastic properties of monoclinic $ZrO_2$. *Phys. B+C* **1988**, *150*, 230–233. [CrossRef]
69. Dalton, J.; Janes, P.; Jones, N.; Nicholson, J.; Hallam, K.; Allen, G. Photocatalytic oxidation of NOx gases using $TiO_2$: a surface spectroscopic approach. *Environ. Pollut.* **2002**, *120*, 415–422. [CrossRef]
70. Liu, X.; Fu, J. Electronic and elastic properties of the tetragonal anatase $TiO_2$ structure from first principle calculation. *Optik* **2020**, *206*, 164342. [CrossRef]
71. Burdett, J.K.; Hughbanks, T.; Miller, G.J.; Richardson Jr, J.W.; Smith, J.V. Structural-electronic relationships in inorganic solids: powder neutron diffraction studies of the rutile and anatase polymorphs of titanium dioxide at 15 and 295 K. *J. Am. Chem. Soc.* **1987**, *109*, 3639–3646. [CrossRef]
72. Arlt, T.; Bermejo, M.; Blanco, M.; Gerward, L.; Jiang, J.; Olsen, J.S.; Recio, J. High-pressure polymorphs of anatase $TiO_2$. *Phys. Rev. B* **2000**, *61*, 14414. [CrossRef]